Carbonyl and defect of metal-free char trigger electron transfer and $O_2^{\bullet-}$ in persulfate activation for Aniline aerofloat degradation

Hailan Yang [a], Rongliang Qiu [b,c,d], Yetao Tang [b,e], Shujing Ye [f], Shaohua Wu [g], Fanzhi Qin [a], Ling Xiang [a], Xiaofei Tan [a,*], Guangming Zeng [a,*], Ming Yan [a]

[a] College of Environmental Science and Engineering and Key Laboratory of Environmental Biology and Pollution Control (Ministry of Education), Hunan University, Changsha 410082, PR China
[b] School of Environmental Science and Engineering, Sun Yat-sen University, Guangzhou 510275, PR China
[c] Guangdong Laboratory for Lingnan Modern Agriculture, Guangzhou 510642, PR China
[d] Guangdong Provincial Key Laboratory of Agricultural & Rural Pollution Abatement and Environmental Safety, College of Natural Resources and Environment, South China Agricultural University, Guangzhou 510642, PR China
[e] Guangdong Provincial Key Lab of Environmental Pollution Control and Remediation Technology, Sun Yat-sen University, Guangzhou 510275, PR China
[f] School of Resources, Environment and Materials, Guangxi University, Nanning 530004, PR China
[g] Guangdong Provincial Key Laboratory of Petrochemical Pollution Processes and Control, Key Laboratory of Petrochemical Pollution Control of Guangdong Higher Education Institutes, School of Environmental Science and Engineering, Guangdong University of Petrochemical Technology, Maoming, Guangdong 525000, PR China

ARTICLE INFO

ABSTRACT

Residual flotation reagents in mineral processing wastewater can trigger severe ecological threats to the local groundwater if they are discharged without treatment. Metal-free biochar-induced persulfate-advanced oxidation processes (KCBC/PS) were used in this study to elucidate the degradation of aniline aerofloat (AAF) – a typical flotation reagent. In KCBC/PS system, AAF can be removed at low doses of catalyst (KCBC, 0.05 g/L) and oxidant (PS, 0.3 mM) additions with high efficiency. The analysis revealed the dominance of $O_2^{\bullet-}$ among the identified reactive oxygen species (ROS), which achieved deeper mineralization for the AAF degradation in the KCBC/PS system. The role of the electron transfer mechanism was equally important; the importance was corroborated by the chemical quenching experiments, electron spin resonance (ESR) detection, probe experiments, and electro-chemical analysis. It benefited from the electron transfer mechanism in the KCBC/PS system and exhibited a wide pH adaptation (3.5–11) and high resistance to inorganic anions for real mining wastewater treatment. Combined with theoretical calculations and other analyses, the carbonyl group was deemed to be the active site of the non-radical pathway of biochar, while the site of the conversion of $SO_4^{\bullet-}$ to superoxide radicals by biochar activation represented a defect. These findings revealed a synergistic effect of multiple active sites on PS activation in biochar-based materials. Moreover, the intermediate degradation products of AAF from mass spectrometry indicated a possible pathway through the density functional theory (DFT) method, which was effective in reducing the environmental toxicity of pollutants for the first time according to the T.E.S.T software and seed germination experiments. Overall, our study proposed a novel modification strategy for cost-effective and environmentally friendly biochar-based catalysts, while also deepening our understanding of the mechanism of activation of persulfate by metal-free carbon-based materials.

1. Introduction

The total volume of non-ferrous metal industry wastewater associated with mining industry arguably account for ~30% of the global discharged wastewater. It contains a large amount of excess organic reagents for collecting, foaming, activating, inhibiting, and dispersing, etc. (Kang et al., 2017; Li et al., 2021a; Lin et al., 2016; Meng et al., 2018) and must be, therefore, effectively treated given its extremely adverse impacts on the technical parameters of the flotation process or poses a serious threat to the ecosystem (Huang et al., 2021; Kang et al., 2017). Aniline aerofloat (AAF, dianilinodithiophosphoric acid, $(C_6H_5NH)_2PSSH$) is a typical organic flotation collector used in mineral

---

processing processes (Deng et al., 2019; Lin et al., 2016). AAF is difficult to degrade naturally and is prone to generate toxic secondary pollutants, posing high ecological risks.

Given their high degradation efficiency and convenient operation in the treatment of organic-polluted water, persulfate (PS)-based advanced oxidation processes (AOPs) are widely used in water treatment processes (Liang et al., 2021; Wu et al., 2021). However, the decomposition rate of persulfate (PS) is slow and must be accelerated by catalysts to produce reactive oxygen species (Cai et al., 2021; Wang and Wang 2018; Ye et al., 2020). Metal-free carbon materials stand out with no metal leaching, acid and alkali resistance, and biocompatibility. Moreover, they have been deemed as excellent catalysts for PS activation, which are not inferior to traditional metal-based catalysts (Sun et al., 2012; Yu et al., 2020a; Yu et al., 2020b).

Of such materials, biochar-based materials clearly stand out with carbon sequestration potential, which made them popular for achieving carbon neutralization and environmental pollution remediation. Although previous studies have unveiled the potential of biochar in PS activation for the treatment of polluted water (Ye et al., 2020; Yu et al., 2020b), the formation and transformation of reactive oxygen species (ROS) in metal-free biochar/persulfate systems both remain unclear. Moreover, the studies on the application potential of biochar/PS systems in the remediation of polluted groundwater in mining areas are scanty. In this light, the biological toxicity and persistence of their intermediate products in the degradation process remained unexplored. Therefore, the degradation mechanisms of AAF in metal-free biochar/PS systems and their pathways require thorough examination and evaluation.

This study mainly aimed to develop a metal-free biochar/PS system for the degradation of AAF in mining wastewater. To this end, we (1) evaluated the degradation pathway and the ROSs in the KCBC/PS system; (2) investigated the active sites of KCBC (metal-free biochar in our study) in PS activation and their effects on ROS formation; (3) identified the oxidation products of AAF by gas chromatography-mass spectrometry (GC–MS), liquid chromatography mass spectrometry (LC-MS), and proposing the degradation pathways evaluated by DFT calculation; and (4) assessed the toxicity of degradation intermediates of AAF by seed germination experiments and T.E.S.T software simulations.

2. Materials and methods

2.1. Synthesis of catalyst

Coffee grounds were collected from a coffee chain brand. They were subsequent dried and pyrolyzed at 300 °C in a tube furnace; the resulting black powders were mashed and shifted through 100 mesh and named coffee biochar. The biochar modification method from previous studies was used in this study (Chen et al., 2021; Qu et al., 2021) with some improvements. In brief, the KOH and coffee biochar were mixed fully using a ball grinding mill (DROIDE, PM 0.4 L, Shanghai), while the mixture was pyrolyzed at 800 °C for 2 h under N$_2$ atmosphere. The obtained powders were washed several times with 1 M HCl and deionized water to remove residual alkali; the obtained biochar is hereafter referred to as KCBC (detailed in Text S1). For comparison, the operation of coffee biochar, except for KOH modification, is denoted as CBC.

2.2. Experimental procedures

The catalytic degradation of KCBC or CBC was performed in a 100 mL flask in a thermostatic shaker at the shaking rate of 150 rpm. The typical process was followed, according to which the catalyst was 0.05 g/L, and the initial concentration of AAF was 20 mg/L. The final PS concentration in the system was 0.3 mM with the addition of a certain amount of PS stock solution to trigger the degradation reaction. Following the set sampling time, the samples were subsequently filtered using 0.22 μm polyvinylidene fluoride (PVDF) disposable filters. Sodium thiosulfate was utilized for the termination reaction. All experiments

repeated at least three times.

2.3. Chemical reagents and analytical methods

Specific information on the materials and chemicals used is summarized in Text S2, while the characterization methods are summarized in Text S3. The residual concentration of Aniline aerofloat (AAF) in solution was detected by high-performance liquid chromatography (HPLC) (Text S4), the degradation intermediates of AAF in KCBC/PS system were pretreated (Text S5 and subsequently observed with Gas chromatography-mass spectrometry (GC-MS) (Text S6) and ultra-high-performance liquid chromatography-mass spectrometry (LC-MS) (Text S7). Electrochemical tests and galvanic oxidation processes were both utilized to elucidate the existence of the non-radical pathway of the system (Text S8). The toxicity evaluation of AAF and its degradation products in the KCBC/PS system were both performed using the Toxicity Estimation Software Tool (T.E.S.T.) program (T.E.S.T. V 4.2.1) (Text S9) and phytotoxicity test (Text S10).

2.4. Theoretical calculation

Quantum chemistry-related calculations were performed in Gaussian 16 based on the density functional theory (DFT) (Grimme et al., 2011; Hariharan and Pople 1973). The geometry optimizations were conducted using the B3LYP functional with a 6–31G(d) basis set for all the atoms. The transition states were performed using the same method and basis set; they were also conducted to ensure that the transition state could connect two related minimums. The structures were optimized, and the high-precision single-point energies were evaluated using the M06–2X functional with a 6–311+G(d,p) basis set for all atoms (Binkley et al., 1980; Yan and Truhlar 2008; Zhao and Truhlar 2008). Solvation effects were considered and the PCM implicit solvation model was applied to this end (Barone and Cossi 1998). Moreover, the Fukui function (f(r)) was introduced to analyze the vulnerable sites of the AAF. These data were used to predict AAF sites during oxidation. For post-processing and visualization, Multiwfn 3.8, GaussView 6.0, and Visual Molecular Dynamics (VMD) 1.9.3 were used (Humphrey et al., 1996; Lu and Chen 2012; Lu and Chen 2020).

The first-principles calculations were performed using the Vienna Ab initio Simulation Package (VASP) within the generalized gradient approximation (GGA) using the Perdew (Burke) Ernzerhof functional. Note that the details of the theoretical calculations are summarized in Text 11–12.
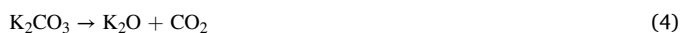
3. Results and discussion

3.1. Material characterizations

First, SEM was used to characterize the morphology and structure of the KCBC and CBC, as shown in Supplementary Fig. S S1. As observed, the surface of the CBC was smooth, with few folds and nearly no holes. The KOH modification caused an apparent change in the microstructure of the KCBC, while the pores of irregular sizes were identified in KCBC, and their surfaces became rough. The N$_2$ adsorption-desorption isotherms and porosity distributions of CBC and KCBC are shown in Supplementary Fig. S S2. As observed, KCBC (S$_{BET}$ = 870.62 m^2/g) with abundant micropore and mesoporous structure (Supplementary Fig. S S2d) exhibited a higher porosity than CBC (S$_{BET}$ = 235.20 m^2/g), which can be ascribed to the KOH inserted and fixed in the pores after ball milling, which further corroded the biochar, thus expanding the surface area. The gasses produced during pyrolysis including CO and CO$_2$ played a pore-forming role, thereby inducing the replacement of the original mesopores and macropores with micropores.

The possible reactions are as follows:

$$KOH + C\text{-}Biochar \rightarrow K + H_2 + K_2CO_3 \tag{1}$$

$$K_2CO_3 + C\text{-Biochar} \rightarrow K_2O + 2CO \tag{2}$$

$$K_2O + C\text{-Biochar} \rightarrow 2K + CO \tag{3}$$

$$K_2CO_3 \rightarrow K_2O + CO_2 \tag{4}$$

$$K + CO_2 \rightarrow K_2O + CO \tag{5}$$

Supplementary Fig. S S2c shows that the adsorption-desorption curve of KCBC matched that of the type I, which corroborates its microporous structure. The CBC curve revealed the type II, stemming from mesopores and macropore structures. The pore distributions of the KCBC and CBC are presented in Supplementary Fig. S S2d. After the modification with KOH, the pore size of KCBC was mainly below 5 nm, and the average pore size was ~2.08 nm, as indicated by Table S1. Moreover, the micropore and mesopore volumes and areas of KCBC were ~3–4 times that of CBC, being driven by the KOH corrosion during pyrolysis. Notably, these findings are in line with the adsorption-desorption curve. Moreover, previous studies and the current results both indicate the KOH activation can produce biochar with a high surface area and large micropores volume (Cai et al., 2021; Qu et al., 2021).

The results of elemental analysis and XPS full spectra, shown in Supplementary Fig. S S3 indicate that the main elements of biochar derived from coffee grounds pyrolysis at high temperatures were C, H, and O, accompanied by negligible N. This pattern was further corroborated by the elemental analysis results (Table S2). Fig. 1 illustrates the analysis of the specific peak information of KCBC and CBC. As observed, four fitted peaks in the high-resolution spectrum of C1s in KCBC were discerned Fig. 1a). They were observed at 284.8, 286.3, 288.5, and 290.6 eV, thus corresponding to C graphite/C-C/C-H, C-O (epoxy and alkoxy) bonds, C=O, and π-π* shake-up in the biochar structure, respectively. However, no C=O bonds were identified in the high-resolution XPS spectra of C1s and O1s of CBC. The FTIR spectra also indicated the low content of C=O in CBC and its relative abundance in KCBC (Supplementary Fig. S S4). As carbonyl and ketone groups have demonstrated to be the active sites for triggering advanced oxidation processes, the poorer catalytic performance of CBC with fewer functional groups than KCBC can be attributed to this pattern. Moreover, KOH modification during pyrolysis significantly enhanced the oxygen content and carbonyl ratio of the biochar. Fig. 1 also shows that the

decreased C=O content in KCBC after PS activation progressed in the system, thus suggesting that C=O represented a potential active site for PS activation (Li et al., 2021b; Liu et al., 2020; Xiao et al., 2022). PS obtained electrons by approaching C=O (Liu et al., 2020), thus crossing the energy barrier to achieve activation (Eqs. (6)-(8)). Furthermore, the slightly increasing proportion of π-π* shake-up in KCBC after the reaction may have stemmed from the small adsorption amount of AAF and the intermediate products. They could be removed by simple ethanol washing to restore the catalytic degradation efficiency of KCBC (Supplementary Fig. S S5).

The XRD results are shown in Supplementary Fig. S S2a. The broad diffraction peak at 20–25° was attributed to the amorphous carbon of biochar (Zhang et al., 2019). After the modification, the characteristic peak of amorphous carbon in biochar was slightly inconspicuous, thus indicating that the crystal shape of the biochar became more prominent after the modification. Furthermore, the carbon skeleton of the biochar was unveiled by the Raman spectra. The peaks located at ~1350 cm^{-1} and ~1585 cm^{-1} represented typical D and G bands, respectively. These peaks were attributed to the defect sites or disordered carbons and were associated with the in-plane stretching vibration of the honeycomb-like sp^2-hybridized carbon. Moreover, the 2D band (~2680 cm^{-1}) could signify a graphitic carbon. The I_D, I_G, and 2D band intensities of KCBC were found higher than those of CBC were. Highly porous KCBC may be obtained at the expense of graphitization in the biochar structure. The I_D/I_G value is the proportion of the number and clusters of aromatic rings, rather than the ratio of sp^3 to sp^2 components. The increased intensity of the D peak can be attributed to the abundant pores of KCBC, which are generally terminated by hydrogen bonds or hanging with other functional groups (Yu et al., 2020b). Moreover, no prominent difference between the I_D/I_G values of KCBC and CBC was discerned. The high-resolution transmission electron microscope (HRTEM) (Supplementary Fig. S S6) further unveiled distinct lattice fringes with an interlayer spacing of ~0.34 nm image of KCBC (Supplementary Fig. S S6b). These results are consistent that of the (002) plane of graphite. Compared with CBC (Supplementary Fig. Ss S6c and d), the regular lattice arrangement further corroborated the high degree of graphitization of KCBC.
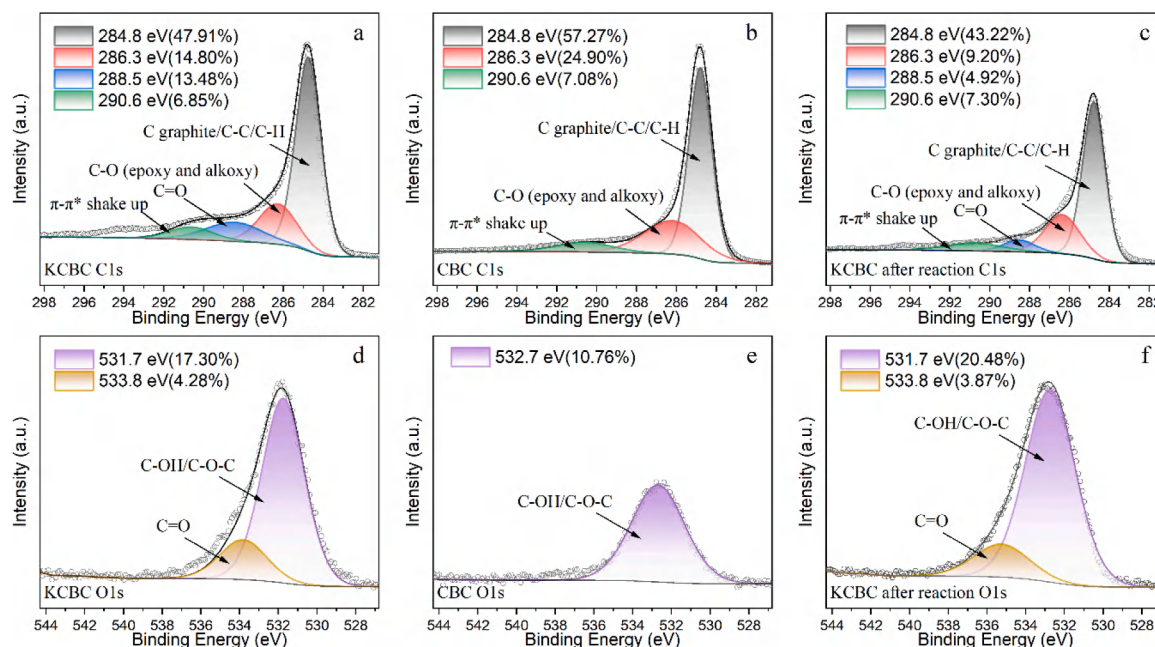

Fig. 1. The high-resolution C 1 s XPS spectrum of (a) KCBC, (b) CBC and (c) KCBC after reaction, the high-resolution O 1 s XPS spectrum of (d) KCBC, (e) CBC and (f) KCBC after reaction.

3.2. Evaluation of PS activation performance

Fig. 2c shows that only a negligible AAF removal proportion was discerned in the individual CBC, PS, and their combination systems. Furthermore, KCBC exhibited a strong activation ability for PS decomposition with a weak adsorption ability. With low material and PS contents, the KCBC/PS system exhibited high AAF degradation efficiency. A slightly difference between the final degradation efficiency of adding the catalyst and oxidant to an AAF solution simultaneously was observed (Fig. 2a), PS was added to an AAF system with adsorption-saturated KCBC (Fig. 2b). This may be attributed to the common active sites for adsorption and degradation of the KCBC/PS system. Moreover, the decreasing reaction rate of AAF in the cycling experiments confirmed the active site competition and irreversible structural changes in KCBC. This can be attributed to the strong adsorption of some intermediates by KCBC, which was further confirmed by the new peaks of N and P in the XPS spectra of KCBC after the reaction (Supplementary Fig. S S3).

AAF is a type of mining trapping agent for lead-zinc sulfide ore; it is usually utilized under weak alkalinity conditions with good selectivity. The KCBC/PS system exhibited good AAF degradation efficiency over a wide pH range, as shown by Fig. 2d. The pKa of the AAF was calculated using ACD Labs (ACD/Percepta 14.52.0). Table S3 shows that the amidogen (-NH-) and sulfhydryl (-SH) of AAF were potential hydrogen ion donors, thereby suggesting that the AAF molecule in the system at the initial pH is deprotonated, and the AAF anion represented the main form. Supplementary Fig. S S7 illustrates the results of the zeta potentials of KCBC tested at different pH values. As observed, the isoelectric point value of KCBC was ~8.7, thereby implying that KCBC was positively charged at pH < 8.7, and negatively charged at pH > 8.7. In the reaction system, KCBC and AAF exhibited opposite electric properties, and the accumulation of pollutants and persulfate ions from the solution to the surface of the material was beneficial to the reaction. The slightly weakened degradation efficiency and k_{obs} of the KCBC/PS system at low pH (initial pH = 3.5, which decreased with the reaction) was potentially driven by the lack of electrostatic attraction between the AAF molecule and KCBC because AAF is neutral. The isoelectric point value of CBC (~3.4) can be another reason for the low degradation efficiency of CBC/PS system for AAF (Supplementary Fig. S7).

The actual oxidation capacity of SR-AOPs is generally affected by the coexistence of substances, such as anions and organic matter. Common anions in groundwater, including $H_2PO_4^-$, HPO_4^{2-}, HCO_3^-, and CO_3^{2-}, and humic acid as the typical natural organic matter, were selected to measure the anti-interference ability for further evaluation. Given the configuration conditions of the simulated pollutant solution, ~300 mM Na^+ and Cl^- were identified, thereby implying that additional Cl^- was not required. The influence of other ions and matter on the anti-jamming capability of the KCBC/PS system was examined under these conditions. It was found that all anions scarcely weakened the AAF degradation efficiency in the KCBC/PS system, which exhibited superior potential for application in highly saline water. The degradation efficiency (degradation rate) and apparent rate constant (k_{obs}) in KCBC/PS with different conditions were further analyzed by SPSS, the result shown in Supplementary Fig. S S8. Different initial pH of AAF solution or with the additional of anions influence the KCBC/PS system has little effect on the degradation rate of KCBC/PS system and has influence on the apparent rate constant. The degradation efficiency of the KCBC/PS system was significantly affected by the AAF solution deviation from the neutral pH (Supplementary Fig. S S9). But at the same initial pH of AAF/KCBC/PS system, no significant difference results were found between the presence or absence of anions. The suppression effect of humic acid can be attributed to the competition between HA and AAF on the KCBC surface.

3.3. Identification of ROS

To further elucidate the contributed ROS in the KCBC/PS system for AAF degradation, MeOH and IPA (propan-2-ol), two quenching scavengers, were first applied for the quenching of $SO_4^{\bullet-}$ ($E(SO_4^{\bullet-} / SO_4^{2-}) = 2.60$ V vs NHE) and $\bullet OH$ ($E(\bullet OH/OH^-) = 2.80$ V vs NHE). Fig. 3a shows that a high proportion of MeOH and IPA [quenching agent: PS = 1000:1] only negligibly affected the KCBC/PS system for AAF degradation, analysis with the EPR detection results and ultimately indicating the possible no effect of $SO_4^{\bullet-}$ and $\bullet OH$ for AAF removal. For contract, there were nearly no free radicals ($SO_4^{\bullet-}$, $\bullet OH$ and $O_2^{\bullet-}$) formation in CBC/PS system (Supplementary Fig. S S13). The addition of DMSO, which had been used for surface-bound radicals, had no influence on the KCBC/PS system. To elucidate the possible non-radical pathway of the KCKC/PS
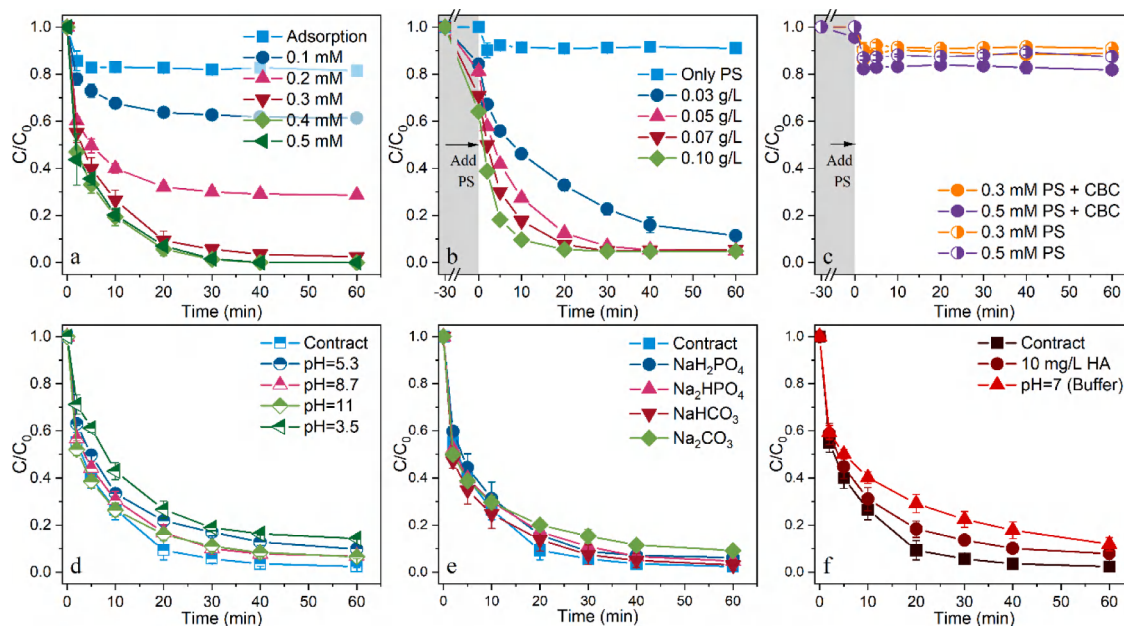

Fig. 2. Effects of (a) PS dosage, (b) KCBC dosage, (c) CBC dosage, (d) initial pH of AAF, (e-f) coexisting organics and inorganics on degradation of AAF. Conditions: [biochar] = 0.05 g/L, [PS] = 0.3 mM, [temperature] = room temperature, [AAF] = 20 mg/L, [initial pH] = 7 ± 0.05.
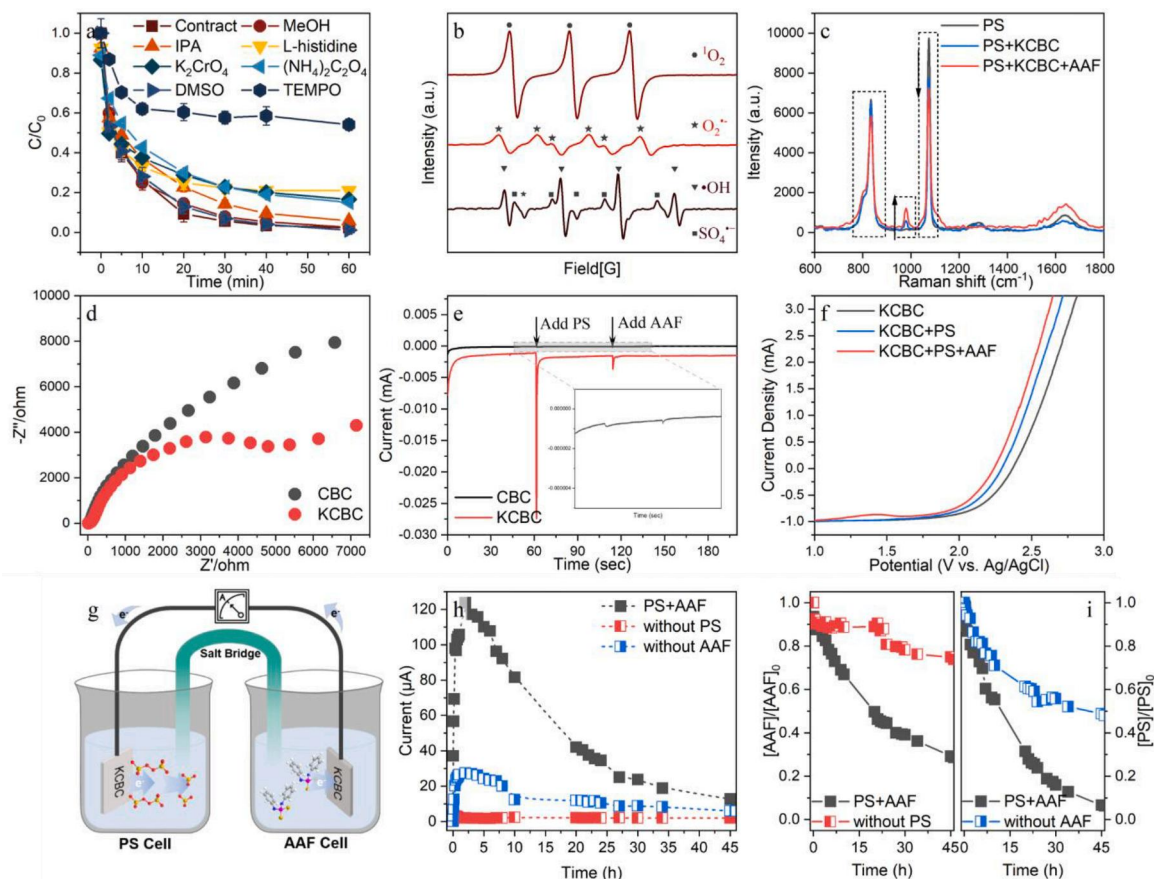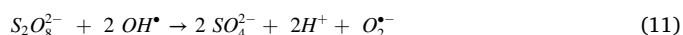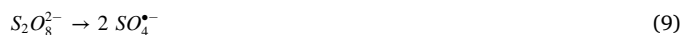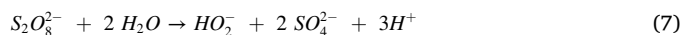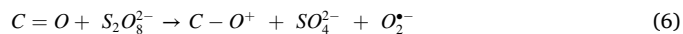
Fig. 3. (a) Influence of different quenching agents, and (b) the ESR detection results of KCBC/PS/AAF system; (c) in situ-Raman of PS, PS+KCBC, and PS+KCBC+AAF; (d) electrochemical impedance spectroscopy (EIS), (e) I-t curves obtained 0 V vs. Ag/AgCl (0.2 M Na$_2$SO$_4$), (f) linear sweep voltammetry (LSV) result of KCBC under different condition. (g) Device setup of galvanic oxidation process (GOP); (h) current flowing from the PS cell to the AAF cell; (i) AAF oxidation and PS decomposing in the GOP system.

system, L-histidine was applied for the quenching of singlet oxygen ($^1O_2$), and < 20% inhibition suggested that $^1O_2$ played a limited role in the KCBC/PS system. The associated intermediate $O_2^{\bullet-}$, which was quenched by 2,2,6,6-Tetramethyl-1-piperidinyloxy (TEMPO), was considered the predominant active substance in the quenching experiments (Fig. 3a). Generally, despite the formation of $O_2^{\bullet-}$ was strongly correlated with that of $^1O_2$, the inhibition by TEMPO was substantially stronger than that by L-histidine or NaN$_3$ at the same molar concentration in the KCBC/PS system. Furthermore, a very weak three-peak signal with equal intensity was ascribed to the generation of 2,2,6,6-tetramethylpiperidine (TEMP). However, no distinct presence of $O_2^{\bullet-}$ was observed by the nitro-blue tetrazolium (NBT) colorimetric method (Text S13 and Supplementary Fig. S 11). The ESR capture experiment demonstrated that the formation of $O_2^{\bullet-}$ in the KCBC/PS system was rapid during the initial reaction stage (Supplementary Fig. S S12c). As $O_2^{\bullet-}$ is generally regarded as generated from excited oxygen molecules, the KCBC/PS/AAF system may have significantly affected the atmospheric environment of the reaction system (Xiao et al., 2022) (Supplementary Fig. S12a). Being a free radical, $O_2^{\bullet-}$ can act as an electron acceptor, thus implying that and slight inhibition with the addition of (NH$_4$)$_2$C$_2$O$_4$ may result from the capture of $O_2^{\bullet-}$ in the reaction system (Wen et al., 2022). Unexpectedly, there no distinct difference in the apparent rate constant and final removal efficiency was discerned between the N$_2$ and O$_2$ injection systems, thus indicating that O$_2$ did not participate in the PS activation process. These findings further suggest that an oxidizing agent acted as a source of $O_2^{\bullet-}$, rather than dissolved oxygen in the solution, while non-radical pathways still existed in the KCBC/PS/AAF system. Delocalized electrons are fundamentally closely

related to $O_2^{\bullet-}$ formation (Li et al., 2021c). Massive carbon defects on the biochar were exacerbated by the KOH activation process, thus facilitating the generation of delocalized electrons at the defective sites; the latter was attributed to $O_2^{\bullet-}$ formation.

Previous studies have confirmed that S$_2$O$_8^{2-}$ can be adsorbed onto the carbonyl groups on the carbon surface to generate $^1O_2$ after several reactions, and there is a transformation between $^1O_2$ and $O_2^{\bullet-}$ (Cheng et al., 2017; Tian et al., 2022). The contribution of $O_2^{\bullet-}$ (the main free radical) for AAF degradation in KCBC/PS system was calculated based on the research of Zhang et al. (2021) (detailed in Text S14–15). Alternatively, $O_2^{\bullet-}$ can be formed by the hydrolysis of PS or monovalent reduction of O$_2$. The $O_2^{\bullet-}$ formation pathway may be based on the following reaction:

$$C = O + S_2O_8^{2-} \rightarrow C - O^+ + SO_4^{2-} + O_2^{\bullet-} \tag{6}$$

$$S_2O_8^{2-} + 2H_2O \rightarrow HO_2^- + 2SO_4^{2-} + 3H^+ \tag{7}$$

$$HO_2^- \rightarrow O_2^{\bullet-} + H^+ \tag{8}$$

$$S_2O_8^{2-} \rightarrow 2SO_4^{\bullet-} \tag{9}$$

$$SO_4^{\bullet-} + H_2O \rightarrow SO_4^{2-} + H^+ + OH^\bullet \tag{10}$$

$$S_2O_8^{2-} + 2OH^\bullet \rightarrow 2SO_4^{2-} + 2H^+ + O_2^{\bullet-} \tag{11}$$

$$O_2^{\bullet-} + OH^\bullet \rightarrow {}^1O_2 + OH^- \tag{12}$$

The consumption of PS in the different systems was monitored for a deeper understanding of KCBC/PS mechanism (Fig. 4). For the KCBC/PS
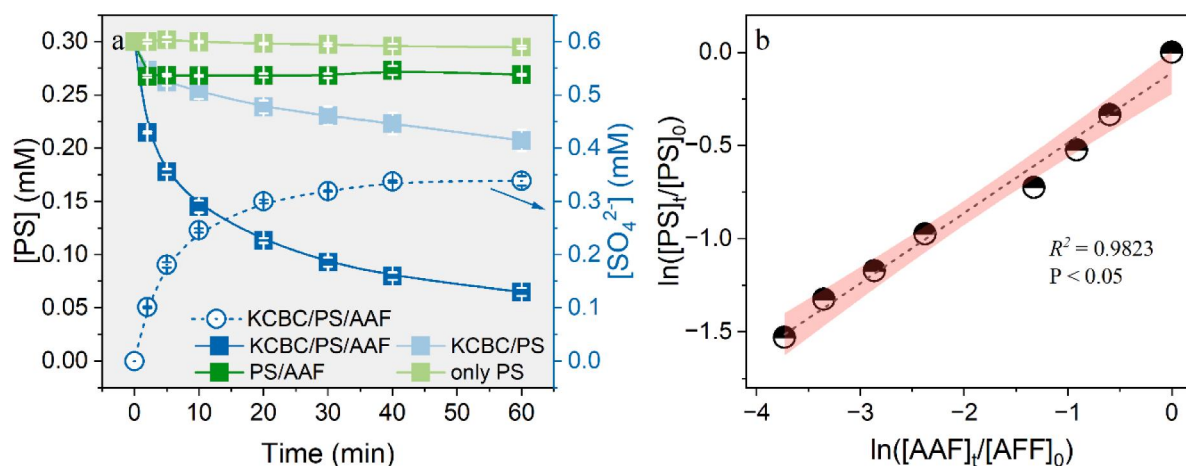
Fig. 4. (a) PS residue concentration and generated SO_4^{2-} in different systems. (b) PS utilization efficiency. [AAF] = 20 mg/L, [PS] = 0.3 mM, [KCBC] = 0.05 g/L, [initial pH] = 7 ± 0.1.

system, the PS conversion rate was enhanced by the introduction of AAF, which may have stemmed from the AAF acting as an electron acceptor and, thus effectively initiating the electron transfer process. Moreover, the difference in stoichiometric amounts between PS decomposition and SO_4^{2-} generation further unveiled the formation of KCBC-PS complexes (Fig. 4a) (Wang et al., 2019). Overall, these results indicate a non-radical pathway in the KCBC/PS/AAF system.

3.4. Electron-transfer pathway

Several researches demonstrated that the possibility relationship between the low effect of anions and water matrix and the existence of the nonradical pathway in PS based advanced oxidation system (Dou et al., 2022; Duan et al., 2018; Ho et al., 2019; Peng et al., 2021; Ye et al., 2020). Nonradical pathway in KCBC/PS system contribute to for AAF degradation (calculated based on the method which detailed in Text S15), which is consistent with the result of the limit effect of anions to KCBC/PS system for AAF degradation. To evaluate the electron-transfer pathway in the KCBC/PS system, given its highly oxidizing properties, K_2CrO_4 was used as an electron trapping agent in the photocatalytic field (Ye et al., 2019). Consequently, a quenching effect has been proven in persulfate-based advanced oxidation systems, similar to that from a previous study (Yu et al., 2020b). An inhibitory effect on the KCBC/PS/AAF system somewhat indicated the possible existence of electron-transport processes. A mixing experiment on delayed pollutant addition was further conducted for investigation. Supplementary Fig. S S14b shows that the removal rate of AAF was slightly weakened with the increase of the time interval of delayed contaminant addition. Even after the addition time of the pollutants was extended to 10 min, the removal rate of AAF remained at 50%, thus indicating that the bridging media-tion of the KCBC/PS system was the main contributor to AAF degrada-tion and biochar coordinated the direct transfer of electrons from pollutants to oxidant molecules. The PS electrophilic molecules were pre-adsorbed on the carbon skeleton of the biochar-based catalyst to form a "carbon-PS complex," thus causing the electronic rearrangement, while subsequently prolonging and weakening the O-O bond on the PS molecule and ultimately activating it to a metastable state (Fig. 3c, g-h). Once an electron-rich pollutant was added, the pollutant molecule as the electron donor directly reacted with the metastable PS as the electron acceptor under the mediation of KCBC.

The radical quenching experiment indicated that non-radical degradation pathways with enhanced electron transfer could occur in this KCBC/PS/AAF system. A series of electrochemical experiments was further performed to identify and measure the electron transfer capacity of KCBC. Fig. 3d illustrates that a smaller arc radius in electrochemical

impedance spectroscopy (EIS) detection was discerned for KCBC instead of CBC, thereby revealing the reduced charge transfer resistance and improved electronic conductivity for KCBC. Moreover, the interaction and electron rearrangement between PS and the biochar-based catalyst were further evaluated by the I-t curves (Fig. 3e). The addition of PS or AAF only slightly affected the chronoamperometric current output of the CBC electrode. Significant current responses were discerned in the KCBC system after the injection of PS and AAF. They can be attributed to the strong interactions between the catalyst, oxidizing agent, and AAF, thereby resonating with the linear sweep voltammetry (LSV) results, shown in Fig. 3f. The increased current in the binary and ternary systems implies the formation of a metastable reactive complex during the re-action. Moreover, an electronic flow occurred from the AAF to the sur-face of KCBC in the KCBC/PS/AAF system, thereby indicating an accelerated oxidation reaction and fast electron transfer on KCBC and the importance of a coexisting reaction. During this process, the addition of AAF provided some electrons to accelerate the oxidation reaction, thus inducing the current increase.

In situ Raman spectra were used to reveal the presence or absence of surface-confined species, described above (Chen et al., 2019; Dou et al., 2022; Ren et al., 2019). The peaks of $S_2O_8^{2-}$ were identified at 837 and 1076 cm^{-1}, and the peak centered at 820 cm^{-1} stemmed from the vi-bration of the prolonged O-O bonds (denoted as $S_2O_8^{2-*}$); virtually the only peaks discerned in the PS. The peak at 982 cm^{-1} can be ascribed to SO_4^{2-} (Fig. 3c), thus indicating a certain self-decomposition phenome-non. Moreover, the intensity increased with the addition of KCBC into the PS solution and the KCBC/PS/AAF system, while the peak intensity of $S_2O_8^{2-}$ was the weakest, and the metastable KCBC-PS* intermediate was relatively strong in the presence of AAF in the KCBC/PS system. However, the intensity of the SO_4^{2-} peak increased and that of the $S_2O_8^{2-}$ peak decreased, being potentially driven by the consumption of PS for AAF degradation during the electron transfer. In this process, the activated PS* with a prolonged peroxide O−O bond exhibited a higher activity to subtract electrons from the electron donor (AAF), thereby yielding the breakup of the O−O bond and decomposition into SO_4^{2-} (Ren et al., 2019). Furthermore, KCBC-mediated electron transfer from AAF to PS may also contribute to AAF oxidation.

The galvanic oxidation process (GOP) device consisted of two half-cells connected by an agarose bridge, and an ammeter was applied to connect two graphite electrodes loaded with KCBC, thus elucidating the current during the reaction in this way (Fig. 3g). Two half cells were used to separate the PS and AAF solutions, whereas the electron transfer pathway, rather than other radical pathways, was further confirmed. Fig. 3h and i revealed no distinct current or AAF degradation in the control system (without PS). However, a significant increase in the

current was discerned in the KCBC and AAF coexisting systems. Furthermore, the current value quickly reached a maximum and then gradually declined throughout the reaction. These findings agree well with the competition kinetics experiments, namely, with the addition of $KCrO_4$, in which the KCBC enhanced the non-radical electron-transfer pathway. Although a similar result was obtained from the PS-only system, the maximum current of the KCBC and AAF coexisting system was six times higher than that of the PS system alone. At the same time, the AAF oxidation efficiency in the GOP system was found to be > 70%, with few adsorption phenomena observed, thereby indicating that AAF can be oxidized by direct electron transfer.

To further evaluate the potential reactive sites and key ROS formation progress in the KCBC/PS system, the Vienna Ab initio Simulation Package (VASP) was used, and the structure of biochar was simplified in further discussion (Momma and Izumi, 2011). Note that the detailed computational method is summarized in Text S12. The conversion pathways of sulfate radicals into other reactive oxygen species (ROS), especially •OH and •OOH, were investigated. To this end, the Gibbs free energies of the reactions were calculated under different conditions. The reaction occurring on the surface of the catalyst can be divided into the following successive reactions:

$$O_2 + H_2O + e^- \rightarrow OOH^* + OH^- \tag{13}$$

$$OOH^* + e^- \rightarrow O^* + OH^- \tag{14}$$

$$O^* + H_2O + e^- \rightarrow OH^* + OH^- \tag{15}$$

$$O_2 + 2H_2O + 4e^- \rightarrow 4OH^- \tag{16}$$

By considering the electron transfer efficiency in the simplified biochar structure, the system work function decreased in the presence of sulfate radicals. This indicates the enhanced electron conductivity, which promoted the electron transfer during the activation of PS (Fig. 5c and d). The Gibbs free energies calculated for the reaction processed, described in Eq-s. 13–16, were used to elucidate the effect of the conversion and catalytic process of reactive oxygen species in the presence or absence of $SO_4^{\bullet-}$ at the two active sites (carbonyl or vacant sites) on the simplified biochar structure. The presence of sulfate radicals can significantly reduce the energy of the system, thereby weakening the energy barrier of the decisive step and play a role in promoting the reaction (Fig. 5). As shown in Fig. 5b, the presence of $SO_4^{\bullet-}$ facilitated the formation of other reactive oxygen species around the vacancies of the simplified biochar structure and promotes the above reaction processes. These results indicate that biochar-based materials can provide abundant active sites not only for persulfate activation, but also for the transformation of ROS. Furthermore, PS assisted in the formation of oxygen intermediates and also weakened the energy barrier of the catalytic reaction cycle. These active sites exhibited combined effects on ROS formation and conversion in the KCBC/PS system.

3.5. Identification of degradation products and possible pathways

Total organic carbon (TOC) measurements were further analyzed to estimate the mineralization efficiency of the AAF KCBC/PS system. Supplementary Fig. S S15 shows that the AAF mineralization efficiency was ~75%, thereby indicating that the KCBC/PS system demonstrated excellent mineralization ability for AAF degradation. This also suggests that some intermediates were generated alongside the mineralization into CO_2 and H_2O in the advanced oxidation process. Furthermore, the generated anions (PO_4^{3-} and NO_3^-) can also indicate the complete mineralization of some AAF in the KCBC/PS system (Supplementary Fig. S S16). On this basis, the intermediate degradation of AAF in the KCBC/PS system was analyzed using GC-MS (Fu et al., 2021). Given the possible thermal decomposition of AAF from the injection port of the GC-MS at high temperature, LC-MS was used for the following analysis as well. The intermediate byproducts that were detected are summarized in Table S5.

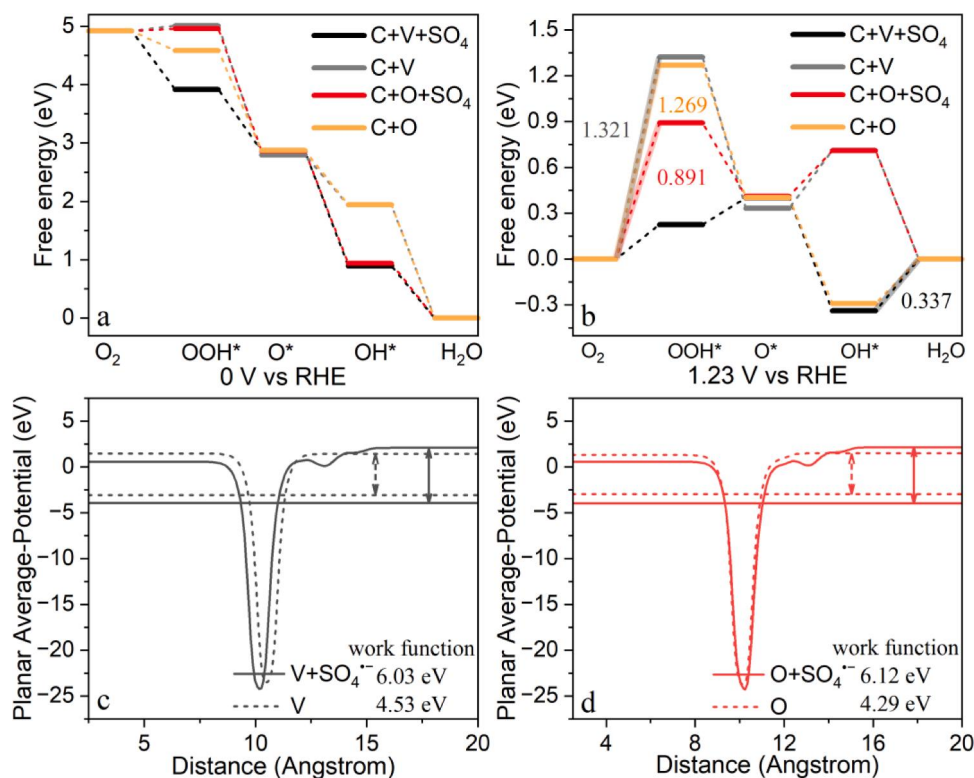Theoretical calculations were used to unveil the AAF degradation

Fig. 5. The calculated Gibbs free energy change of ORR process at (a) $U = 0$ V and (b) $U = 1.23$ V. And the work function (c-d) of simplified biochar structure with or without $SO_4^{\bullet-}$.

pathways in the KCBC/PS system. Fundamentally, the Fukui function is an efficient, widely used method that relies on the Gaussian software to predict reactive sites for different radicals. The optimized chemical structure of the AAF is shown in Fig. 6a. As seen, the electrophilic (f −), radical (f0), and nucleophilic (f +) values theoretically revealed the relative activity of each atom in an AAF molecule. The Fukui function value of f⁻, which can be used to predict the molecular reactivity to radicals attacked by $O_2^{\bullet-}$, was the only electrophilic species detected in this study. The highest f⁻ (electrophilic attack) values of AAF were ~2S (−0.2252), being followed by 3S (−0.698) and 6 N (−0.0686); they were susceptible to attack by $O_2^{\bullet-}$. A specific atom with a high condensed dual descriptors (CDD) value generally exhibits the higher reactivity at the molecular sites. As depicted in Fig. 6d, the 2S atom (−0.0795) and 6 N (−0.0568) exhibited lower CDD value and were closely surrounded by the negative isosurface of the Fukui Index, which indicates that they are priority sites, which is consistent with the conclusion of the Fukui function. Therefore, in our study, the most probable reaction sites of AAF in the KCBC/PS system were around the 1P atom. Fig. 6b and c also illustrate the lowest unoccupied molecular orbital (LUMO) and highest occupied molecular orbital (HOMO) of the AAF molecule. This pattern implies that the regions that can easily lose/add electrons for attack by electrophilic/nucleophilic species. As clearly presented, the HOMO of AAF was mainly located on the N atom of the piperazine ring, S atom, and C atoms in the benzene ring associated with N and S. In our study, aniline (TP1) is supposed to be the initial decomposition product of AAF in KCKC/PS system, with the formation of some low-molecular-weight intermediates containing phosphorus or sulfur (TP8). Subsequent oxidation was carried out to form the intermediates, which are benzene ring substitutes (TP2–5). Furthermore, some of them were subsequently mineralized and anions were formed through subsequent oxidation forms straight chain products (TP7). The possible degradation pathways of AAF using the KCBC/PS system are demonstrated in Supplementary Fig. S16.

By benefiting from the narrow energy gap of KCBC, the electrons localized at the highest occupied molecular orbital (HOMO, −6.355 eV) of AAF can be readily transferred to the lowest unoccupied molecular orbital (LUMO, −1.096 eV) of the metastable PS* complex via the carbon tunnel driven by a potential energy difference. This, in turn, triggers the PS decomposition, during which the PS abstracts two electrons from the AAF instead of acting as a one-electron oxidant to generate $SO_4^{\bullet-}$. These findings in synergy with the aforementioned results from previous sections point on a possible mechanism for AFF oxidation in the KCBC/PS system. More specifically, the possible activation pathways are:

$$S_2O_8^{2-} + 2\ e^-\ (from\ AAF) \rightarrow 2\ SO_4^{2-} \qquad (17)$$
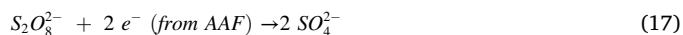
The Toxicity Estimation Software Tool (T.E.S.T), shown in Fig. 7a-f is based on the quantitative structure-activity relationship (QSAR). T.E.S.T. was further used to evaluate the degradation intermediates of AAF in the KCBC/PS system and demonstrated that nearly all the degradation intermediates were not harmful to acute toxicity in aquatic organisms (fathead minnow LC$_{50}$ (96 h), Daphnia magna LC$_{50}$ (48 h), and T. pyriformis IGC$_{50}$ (48 h)). Moreover, there no bioaccumulation or genotoxicity of the assessed degradation intermediates was discerned, where only some intermediates exhibited developmental toxicity. Furthermore, Chinese cabbage seed germination and radicle length, shown in Fig. 7g-h were applied evaluate the toxicity of the intermediates in the KCBC/PS system. The KCBC/PS system can eliminate the toxicity of AAF on the seed germination rate base on the statistical analysis using SPSS Statistics 26.

4. Conclusion

To conclude, this study proposed the large-scale preparation of metal-free biochar-based materials that activate persulfate for the degradation of AAF. The KCBC/PS system exhibited high removal efficiency of AAF at low doses of catalyst (KCBC, 0.05 g/L) and oxidant (PS, 0.3 mM) additions. In the KCBC/PS system, $O_2^{\bullet-}$ was found the dominant reactive oxygen species, which yielded high mineralization rates of >70%. Moreover, the existing electron transfer mechanism provided a good resistance to co-existing ions in the environment. KOH activation endows the biochar with abundant carbonyl functional groups and defective structures as effective active sites for electron transfer
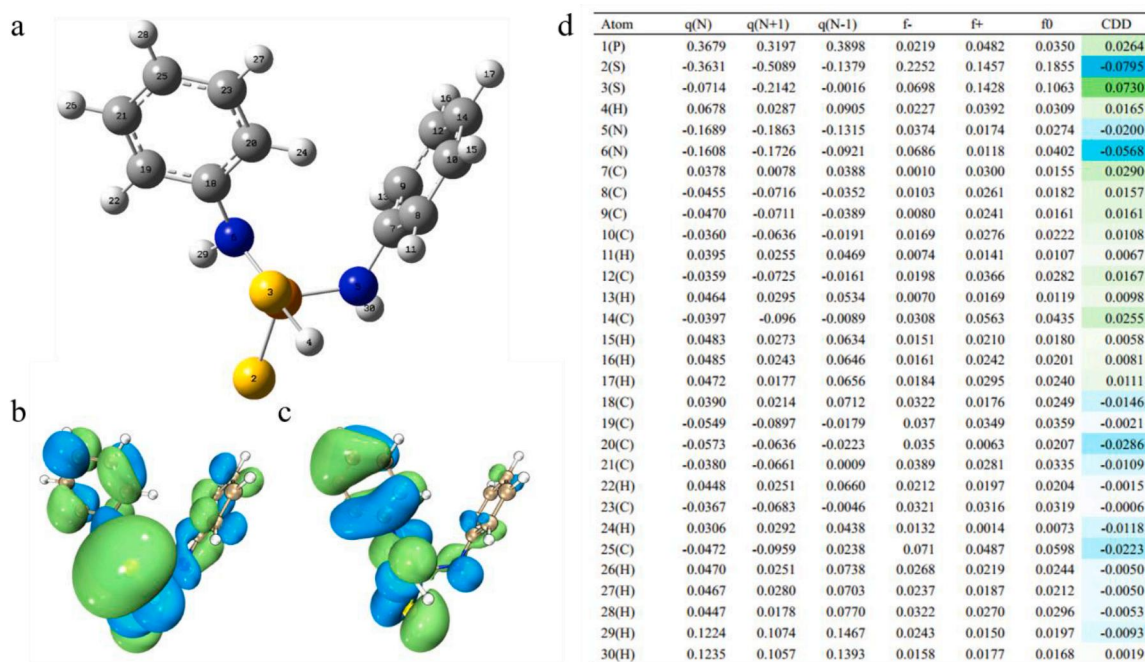

Atom	q(N)	q(N+1)	q(N-1)	f-	f+	f0	CDD
1(P)	0.3679	0.3197	0.3898	0.0219	0.0482	0.0350	0.0264
2(S)	-0.3631	-0.5089	-0.1379	0.2252	0.1457	0.1855	-0.0795
3(S)	-0.0714	-0.2142	-0.0016	0.0698	0.1428	0.1063	0.0730
4(H)	0.0678	0.0287	0.0905	0.0227	0.0392	0.0309	0.0165
5(N)	-0.1689	-0.1863	-0.1315	0.0374	0.0174	0.0274	-0.0200
6(N)	-0.1608	-0.1726	-0.0921	0.0686	0.0118	0.0402	-0.0568
7(C)	0.0378	0.0078	0.0388	0.0010	0.0300	0.0155	0.0290
8(C)	-0.0455	-0.0716	-0.0352	0.0103	0.0261	0.0182	0.0157
9(C)	-0.0470	-0.0711	-0.0389	0.0080	0.0241	0.0161	0.0161
10(C)	-0.0360	-0.0636	-0.0191	0.0169	0.0276	0.0222	0.0108
11(H)	0.0395	0.0255	0.0469	0.0074	0.0141	0.0107	0.0067
12(C)	-0.0359	-0.0725	-0.0161	0.0198	0.0366	0.0282	0.0167
13(H)	0.0464	0.0295	0.0534	0.0070	0.0169	0.0119	0.0098
14(C)	-0.0397	-0.096	-0.0089	0.0308	0.0563	0.0435	0.0255
15(H)	0.0483	0.0273	0.0634	0.0151	0.0210	0.0180	0.0058
16(H)	0.0485	0.0243	0.0646	0.0161	0.0242	0.0201	0.0081
17(H)	0.0472	0.0177	0.0656	0.0184	0.0295	0.0240	0.0111
18(C)	0.0390	0.0214	0.0712	0.0322	0.0176	0.0249	-0.0146
19(C)	-0.0549	-0.0897	-0.0179	0.037	0.0349	0.0359	-0.0021
20(C)	-0.0573	-0.0636	-0.0223	0.035	0.0063	0.0207	-0.0286
21(C)	-0.0380	-0.0661	0.0009	0.0389	0.0281	0.0335	-0.0109
22(H)	0.0448	0.0251	0.0660	0.0212	0.0197	0.0204	-0.0015
23(C)	-0.0367	-0.0683	-0.0046	0.0321	0.0316	0.0319	-0.0006
24(H)	0.0306	0.0292	0.0438	0.0132	0.0014	0.0073	-0.0118
25(C)	-0.0472	-0.0959	0.0238	0.071	0.0487	0.0598	-0.0223
26(H)	0.0470	0.0251	0.0738	0.0268	0.0219	0.0244	-0.0050
27(H)	0.0467	0.0280	0.0703	0.0237	0.0187	0.0212	-0.0050
28(H)	0.0447	0.0178	0.0770	0.0322	0.0270	0.0296	-0.0053
29(H)	0.1224	0.1074	0.1467	0.0243	0.0150	0.0197	-0.0093
30(H)	0.1235	0.1057	0.1393	0.0158	0.0177	0.0168	0.0019

Fig. 6. (a) Chemical structure of AAF after optimization with numbers marked (gray: C; white: H; blue: N; yellow: S), (b) LUMO, and (c) HOMO based on the isosurface of Fukui index (The blue and green colors represent the negative and positive phases of the molecular orbital); (d) Condensed Fukui index distribution on AAF molecule.
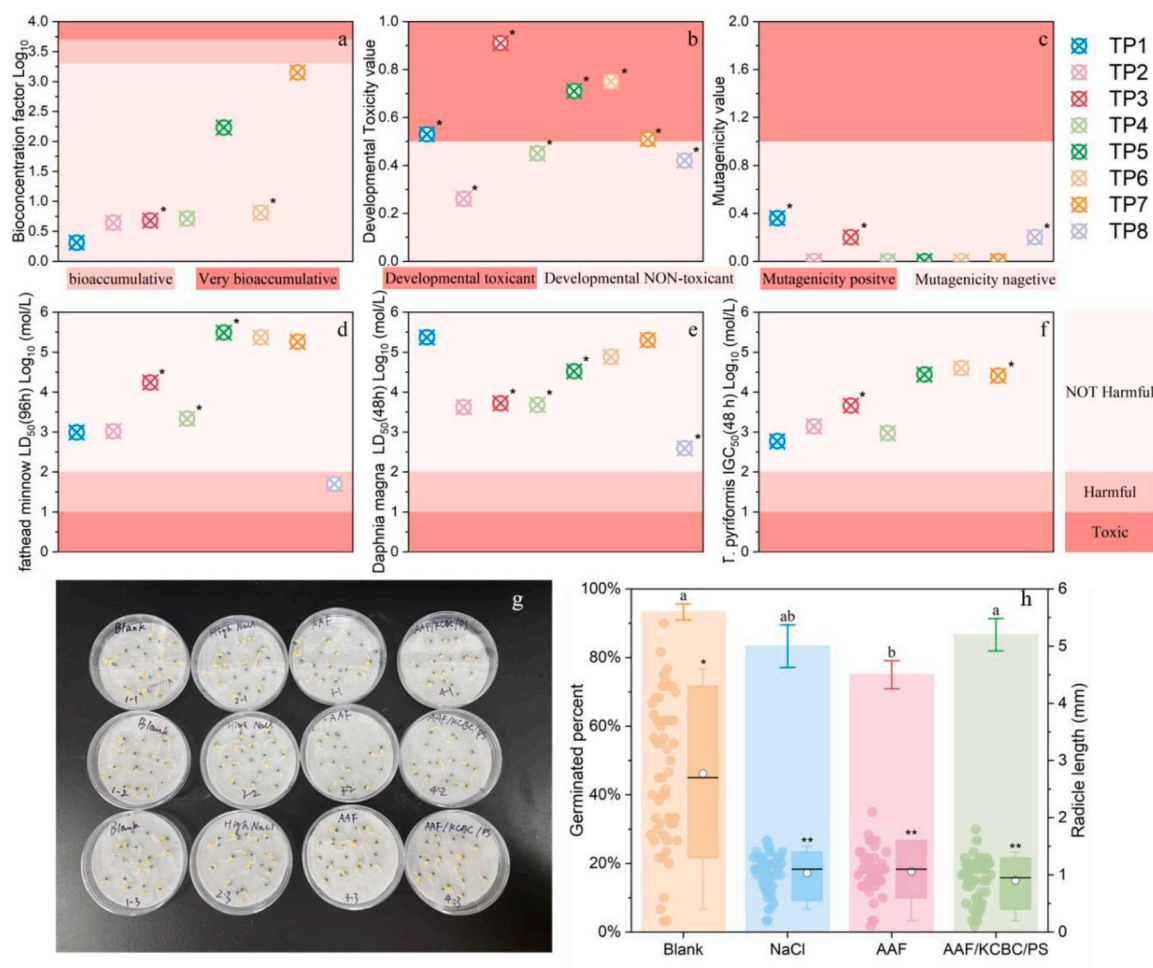
Fig. 7. Theoretically calculated (a) bioconcentration factor, (b) developmental toxicity value, (c) mutagenicity value, and acute toxicity of (d) *Fathead minnow* LC50 (96 h), (e) *Daphnia Magna* LC50 (48 h), and (f) *T. Pyriformis* IGC50 (48 h) degradation intermediates of AAF via T.E.S.T. (* as the label for predicted value rather than experimental value). (g-h) Effect of different samples on Chinese cabbage seed germination and radicle length for 36 h ($n = 60$), Boxes illustrate the first quartile, median and third quartile of the data. The mean is marked with a dotted line in the box. The ends of the whiskers represent the 5th percentile and the 95th percentile and a micrograph of seed radicle on the left.

pathways and superoxide radical formation, respectively. Moreover, it highlights their role in the reactive oxygen species formation and conversion according to the characterization analyses results (including XPS, electrochemistry, electrooxidation, and in-situ Raman testing) and theoretical calculations. The intermediate degradation products and possible degradation pathways of AAF were inferred by calculating the attacked sites of AAF in the system using DFT, combined with mass spectrometry analysis. We further combined the software and seed germination experiments to elucidate the efficiency in reducing the environmental toxicity of pollutants. Our study proposed a modification strategy for cost-effective and environmentally friendly biochar-based catalysts, while also broadening the pathway of persulfate-based AOPs for the treatment of organically contaminated mining and smelting effluents.

Declaration of Competing Interest

The authors declare that they have no known competing financial interests or personal relationships that could have appeared to influence the work reported in this paper.

Data availability

Data will be made available on request.

Supplementary materials

Supplementary material associated with this article can be found, in the online version, at doi:10.1016/j.watres.2023.119659.

References

Barone, V., Cossi, M., 1998. Quantum calculation of molecular energies and energy gradients in solution by a conductor solvent model. J. Phys. Chem. A 102 (11), 1995–2001.
Binkley, J.S., Pople, J.A., Hehre, W.J., 1980. Self-consistent molecular orbital methods. 24. Supplemented small split valence basis sets for 2nd row elements. Chem. Informationsdienst 11 (18).
Cai, S., Zhang, Q., Wang, Z., Hua, S., Ding, D., Cai, T., Zhang, R., 2021. Pyrrolic N-rich biochar without exogenous nitrogen doping as a functional material for bisphenol A removal: performance and mechanism. Appl. Catal. B 291, 120093.

Chen, W.H., Du, J.T., Lee, K.T., Ong, H.C., Park, Y.K., Huang, C.C., 2021. Pore volume upgrade of biochar from spent coffee grounds by sodium bicarbonate during torrefaction. Chemosphere 275, 129999.

Chen, Y., Zhang, G., Liu, H., Qu, J., 2019. Confining Free radicals in close vicinity to contaminants enables ultrafast fenton-like processes in the interspacing of MoS2 membranes. Angew. Chem., Int. Ed. Engl. 58 (24), 8134–8138.

Cheng, X., Guo, H., Zhang, Y., Wu, X., Liu, Y., 2017. Non-photochemical production of singlet oxygen via activation of persulfate by carbon nanotubes. Water Res. 113, 80–88.

Deng, X., Zhang, D., Wu, M., Antwi, P., Su, H., Lai, C., 2019. Enhanced removal of refractory pollutant from aniline aerofloat wastewater using combined vacuum ultraviolet and ozone (VUV/O₃) process. Water Sci. Technol. 80 (12), 2250–2259.

Dou, J., Cheng, J., Lu, Z., Tian, Z., Xu, J., He, Y., 2022. Biochar co-doped with nitrogen and boron switching the free radical based peroxydisulfate activation into the electron-transfer dominated nonradical process. Appl. Catal. B 301, 120832.

Duan, X., Sun, H., Wang, S., 2018. Metal-free carbocatalysis in advanced oxidation reactions. Acc. Chem. Res. 51 (3), 678–687.

Fu, P., Ma, Y., Lei, B., Li, G., Lin, X., 2021. Decomposition of refractory aniline aerofloat collector in aqueous solution by an ozone/vacuum-UV (O3/VUV) process. Environ. Technol. 42 (4), 659–670.

Grimme, S., Ehrlich, S., Goerigk, L., 2011. Effect of the damping function in dispersion corrected density functional theory. J. Comput. Chem. 32 (7), 1456–1465.

Hariharan, P., Pople, J.A., 1973. The influence of polarization functions on molecular orbital hydrogenation energies. Theor. Chim. Acta 28, 213–222.

Ho, S.H., Chen, Y.D., Li, R., Zhang, C., Ge, Y., Cao, G., Ma, M., Duan, X., Wang, S., Ren, N. Q., 2019. N-doped graphitic biochars from C-phycocyanin extracted Spirulina residue for catalytic persulfate activation toward nonradical disinfection and organic oxidation. Water Res. 159, 77–86.

Huang, X., Yu, Y., Chen, H., Liang, H., Geng, M., Shi, B., 2021. Disinfection by-product formation and toxicity evaluation for chlorination with powered activated carbon. Water Res. 205, 117660.

Humphrey, W., Dalke, A., Schulten, K., 1996. VMD - visual molecular dynamics. J. Molec. Graphics 14, 33–38.

Kang, J., Sun, W., Hu, Y., Gao, Z., Liu, R., Zhang, Q., Liu, H., Meng, X., 2017. The utilization of waste by-products for removing silicate from mineral processing wastewater via chemical precipitation. Water Res. 125, 318–324.

Li, M., Zhong, H., He, Z., Hu, L., Sun, W., Loganathan, P., Xiong, D, 2021a. Degradation of various thiol collectors in simulated and real mineral processing wastewater of sulfide ore in heterogeneous modified manganese slag/PMS system. Chem. Eng. J. 413, 127478.

Li, N., Li, R., Duan, X., Yan, B., Liu, W., Cheng, Z., Chen, G., Hou, L., Wang, S., 2021b. Correlation of Active sites to generated reactive species and degradation routes of organics in peroxymonosulfate activation by Co-loaded carbon. Environ. Sci. Technol. 55 (23), 16163–16174.

Li, X., Wang, J., Duan, X., Li, Y., Fan, X., Zhang, G., Zhang, F., Peng, W., 2021c. Fine-tuning radical/nonradical pathways on graphene by porous engineering and doping strategies. ACS Catal. 11 (8), 4848–4861.

Liang, J., Duan, X., Xu, X., Chen, K., Zhang, Y., Zhao, L., Qiu, H., Wang, S., Cao, X., 2021. Persulfate oxidation of sulfamethoxazole by magnetic iron-char composites via nonradical pathways: Fe(IV) versus surface-mediated electron transfer. Environ. Sci. Technol. 55 (14), 10077–10086.

Lin, W., Tian, J., Ren, J., Xu, P., Dai, Y., Sun, S., Wu, C., 2016. Oxidation of aniline aerofloat in flotation wastewater by sodium hypochlorite solution. Environ. Sci. Pollut. Res. Int. 23 (1), 785–792.

Liu, Y., Luo, J., Tang, L., Feng, C., Wang, J., Deng, Y., Liu, H., Yu, J., Feng, H., Wang, J., 2020. Origin of the enhanced reusability and electron transfer of the carbon-coated Mn3O4 nanocube for persulfate activation. ACS Catal. 10 (24), 14857–14870.

Lu, T., Chen, F., 2012. Multiwfn: a multifunctional wavefunction analyzer. J. Comput. Chem. 33 (5), 580–592.

Lu, T., Chen, Q., 2020. van der Waals potential: an important complement to molecular electrostatic potential in studying intermolecular interactions. J. Mol. Model. 26 (11), 315.

Meng, X., Wu, J., Kang, J., Gao, J., Liu, R., Gao, Y., Wang, R., Fan, R., Khoso, S.A., Sun, W., Hu, Y., 2018. Comparison of the reduction of chemical oxygen demand in wastewater from mineral processing using the coagulation–flocculation, adsorption and Fenton processes. Miner. Eng. 128, 275–283.

Momma, K., Izumi, F., 2011. VESTA 3 for three-dimensional visualization of crystal, volumetric and morphology data. J. Appl. Crystallogr. 44, 1272–1276.

Peng, J., Zhou, P., Zhou, H., Liu, W., Zhang, H., Zhou, C., Lai, L., Ao, Z., Su, S., Lai, B., 2021. Insights into the electron-transfer mechanism of permanganate activation by graphite for enhanced oxidation of sulfamethoxazole. Environ. Sci. Technol. 55 (13), 9189–9198.

Qu, J., Wang, Y., Tian, X., Jiang, Z., Deng, F., Tao, Y., Jiang, Q., Wang, L., Zhang, Y., 2021. KOH-activated porous biochar with high specific surface area for adsorptive removal of chromium (VI) and naphthalene from water: affecting factors, mechanisms and reusability exploration. J. Hazard. Mater. 401, 123292.

Ren, W., Xiong, L., Yuan, X., Yu, Z., Zhang, H., Duan, X., Wang, S., 2019. Activation of peroxydisulfate on carbon nanotubes: electron-transfer mechanism. Environ. Sci. Technol. 53 (24), 14595–14603.

Sun, H., Liu, S., Zhou, G., Ang, H.M., Tade, M.O., Wang, S., 2012. Reduced graphene oxide for catalytic oxidation of aqueous organic pollutants. ACS Appl. Mater. Interfaces 4 (10), 5466–5471.

Tian, W., Lin, J., Zhang, H., Duan, X., Wang, H., Sun, H., Wang, S., 2022. Kinetics and mechanism of synergistic adsorption and persulfate activation by N-doped porous carbon for antibiotics removals in single and binary solutions. J. Hazard. Mater. 423 (Pt A), 127083.

Wang, H., Guo, W., Liu, B., Wu, Q., Luo, H., Zhao, Q., Si, Q., Sseguya, F., Ren, N., 2019. Edge-nitrogenated biochar for efficient peroxydisulfate activation: an electron transfer mechanism. Water Res. 160, 405–414.

Wang, J., Wang, S., 2018. Activation of persulfate (PS) and peroxymonosulfate (PMS) and application for the degradation of emerging contaminants. Chem. Eng. J. 334, 1502–1517.

Wen, Y., Yan, J., Yang, B., Zhuang, Z., Yu, Y., 2022. Reactive oxygen species on transition metal-based catalysts for sustainable environmental applications. J. Mater. Chem. A 10 (37), 19184–19210.

Wu, W., Zhu, S., Huang, X., Wei, W., Jin, C., Ni, B.J., 2021. Determination of instinct components of biomass on the generation of persistent free radicals (PFRs) as critical redox sites in pyrogenic chars for persulfate activation. Environ. Sci. Technol. 55 (11), 7690–7701.

Xiao, P., Yi, X., Wu, M., Wang, X., Zhu, S., Gao, B., Liu, Y., Zhou, H., 2022. Catalytic performance and peroxidate activation mechanism of anaerobic sewage sludge-derived biochar. J. Hazard. Mater. 424 (Pt C), 127692.

Yan, Z., Truhlar, D.G., 2008. The M06 suite of density functionals for main group thermochemistry, thermochemical kinetics, noncovalent interactions, excited states, and transition elements: two new functionals and systematic testing of four M06-class functionals and 12 other functionals. Theor. Chem. Acc. 119 (1–3), 525.

Ye, S., Yan, M., Tan, X., Liang, J., Zeng, G., Wu, H., Song, B., Zhou, C., Yang, Y., Wang, H., 2019. Facile assembled biochar-based nanocomposite with improved graphitization for efficient photocatalytic activity driven by visible light. Appl. Catal. B 250, 78–88.

Ye, S., Zeng, G., Tan, X., Wu, H., Liang, J., Song, B., Tang, N., Zhang, P., Yang, Y., Chen, Q., Li, X., 2020. Nitrogen-doped biochar fiber with graphitization from *Boehmeria nivea* for promoted peroxymonosulfate activation and non-radical degradation pathways with enhancing electron transfer. Appl. Catal. B 269, 118850.

Yu, J., Feng, H., Tang, L., Pang, Y., Zeng, G., Lu, Y., Dong, H., Wang, J., Liu, Y., Feng, C., Wang, J., Peng, B., Ye, S., 2020a. Metal-free carbon materials for persulfate-based advanced oxidation process: microstructure, property and tailoring. Prog. Mater Sci. 111, 100654.

Yu, J.F., Tang, L., Pang, Y., Zeng, G.M., Feng, H.P., Zou, J.J., Wang, J.J., Feng, C.Y., Zhu, X., Ouyang, X.L., Tan, J.S., 2020b. Hierarchical porous biochar from shrimp shell for persulfate activation: a two-electron transfer path and key impact factors. Appl. Catal. B 260, 118160.

Zhang, L.S., Jiang, X.H., Zhong, Z.A., Tian, L., Sun, Q., Cui, Y.T., Lu, X., Zou, J.P., Luo, S. L., 2021. Carbon nitride supported high-loading fe single-atom catalyst for activation of peroxymonosulfate to generate (1) O2 with 100% selectivity. Angew. Chem. Int. Ed. Engl. 60 (40), 21751–21755.

Zhang, P., Tan, X., Liu, S., Liu, Y., Zeng, G., Ye, S., Yin, Z., Hu, X., Liu, N., 2019. Catalytic degradation of estrogen by persulfate activated with iron-doped graphitic biochar: process variables effects and matrix effects. Chem. Eng. J. 378, 122–141.

Zhao, Y., Truhlar, D.G., 2008. Density functionals with broad applicability in chemistry. Acc. Chem. Res. 41 (2), 157–167.